

**Electronic Supporting Information for: Single-Molecule Conductance of  
Dibenzopentalenes: Anti-Aromaticity and Quantum Interference.**

Maximilian Schmidt, Daniel Wassy, Mathias Hermann, M. Teresa González, Nicolás Agrait,  
Linda A.Zotti, Birgit Esser and Edmund Leary.

## Content

1	Materials and Methods.....	3
2	Synthetic Manipulations .....	4
2.1	2,7-Dimesityl-5,10-bis((4-(methylthio)phenyl)ethynyl)-4b,5,9b,10-tetrahydroindeno[2,1- <i>a</i> ]indene-5,10-diol ( <b>S4</b> ) .....	6
2.2	2,7-Dimesityl-5,10-bis((4-(methylthio)phenyl)ethynyl)indeno-[2,1- <i>a</i> ]indene ( <b>5</b> ) .....	7
2.3	4-Ethynylthioanisole ( <b>12</b> ) .....	8
2.4	2,7-Bis((4-(methylthio)phenyl)ethynyl)-5,10-dimesityl-5,10-indeno-[2,1- <i>a</i> ]indene ( <b>6</b> ) .....	9
2.5	9,10-Bis((4-(methylthio)phenyl)ethynyl)anthracene ( <b>7</b> ) .....	10
3	NMR spectra .....	11
4	Absorption Spectra .....	15
5	Cyclic Voltammograms .....	15
6	DFT calculations .....	17
6.1	NICS(1) <sub>iso</sub> -calculations .....	17
7	Summary of electrochemical and optical properties.....	18
8	Single Crystal X-Ray Diffraction.....	19
9	STM Breakjunction Measurements .....	22
9.1	Sample preparation for single-molecule experiments.....	22
9.2	Single-Molecule Conductivity Studies.....	22
9.3	Conductance versus voltage behaviour .....	25
10	Transport calculations.....	27
10.1	Technical details .....	27
10.2	DFT-based results for pentalene versus dibenzopentalene cores .....	28
10.3	Tight-binding transport calculations.....	29
11	A note on the relation between aromaticity/antiaromaticity and HOMO-LUMO gap. ...	30
12	References .....	31

# 1 Materials and Methods

## Chemicals and Solvents

Chemicals and reagents were purchased from ACROS-ORGANICS, ALFA-AESAR, CHEMPUR or SIGMA ALDRICH and used directly without further purification unless specified otherwise. Moisture- or oxygen-sensitive reactions were carried out in dried glassware—heated under vacuum—using standard Schlenk techniques in a dry argon atmosphere (Argon 5.0 from SAUERSTOFFWERKE FRIEDRICHSHAFEN). Anhydrous solvents (THF, toluene) were obtained from an M. BRAUN solvent purification system (MB-SPS-800) and stored over activated molecular sieves (3 Å) for several days.<sup>[1]</sup> Cyclohexane for column chromatography was purchased in technical grade and purified by distillation under reduced pressure. Other solvents were purchased and used in analytical grade.

## Analytical Thin Layer Chromatography (TLC)

Thin layer chromatography was carried out using silica gel-coated aluminum plates with a fluorescence indicator (MERCK 60 F<sub>254</sub>). The visualization of spots was achieved using UV-light ( $\lambda_{\text{max}} = 254$  and 366 nm) or KMnO<sub>4</sub> staining solution (3.0 g KMnO<sub>4</sub>, 20 g, K<sub>2</sub>CO<sub>3</sub>, 5.0 mL aq. NaOH (5 wt%), 300 mL H<sub>2</sub>O).

## Flash Column Chromatography

Column chromatography was carried out using silica gel 60 (grain size 40–63  $\mu\text{m}$ ) from MACHERY-NAGEL or aluminum oxide basic 90 from MACHERY-NAGEL.

## Nuclear Magnetic Resonance Spectroscopy (NMR)

NMR spectra were recorded at 300 K using BRUKER Avance III HD [300 MHz (<sup>1</sup>H)], BRUKER Avance II [400.1 MHz (<sup>1</sup>H), 101.6 MHz (<sup>13</sup>C)] and BRUKER Avance III HD [500.3 MHz (<sup>1</sup>H), 125.8 MHz (<sup>13</sup>C)] spectrometers. Chemical shifts are reported in parts per million (ppm,  $\delta$  scale) relative to the signal of tetramethylsilane ( $\delta = 0.00$  ppm). <sup>1</sup>H NMR spectra are referenced to tetramethylsilane as an internal standard or the residual solvent signal of CDCl<sub>3</sub> ( $\delta = 7.26$  ppm). <sup>13</sup>C NMR spectra are referenced to tetramethylsilane as an internal standard or the solvent signal of CDCl<sub>3</sub> ( $\delta = 77.16$  ppm).<sup>[2]</sup>

The analysis followed first order, and the multiplets were abbreviated using the following codes: singlet (s), broad singlet (br), doublet (d), triplet (t), quartet (q), multiplet (m) and combinations thereof, such as doublet of doublets (dd).

## High Resolution Mass Spectrometry (HRMS)

All HRMS spectra were measured on a THERMO FISCHER SCIENTIFIC INC. Exactive via electro spray ionization (ESI) or atmospheric pressure chemical ionization (APCI) with an orbitrap analyzer.

## Cyclic Voltammetry

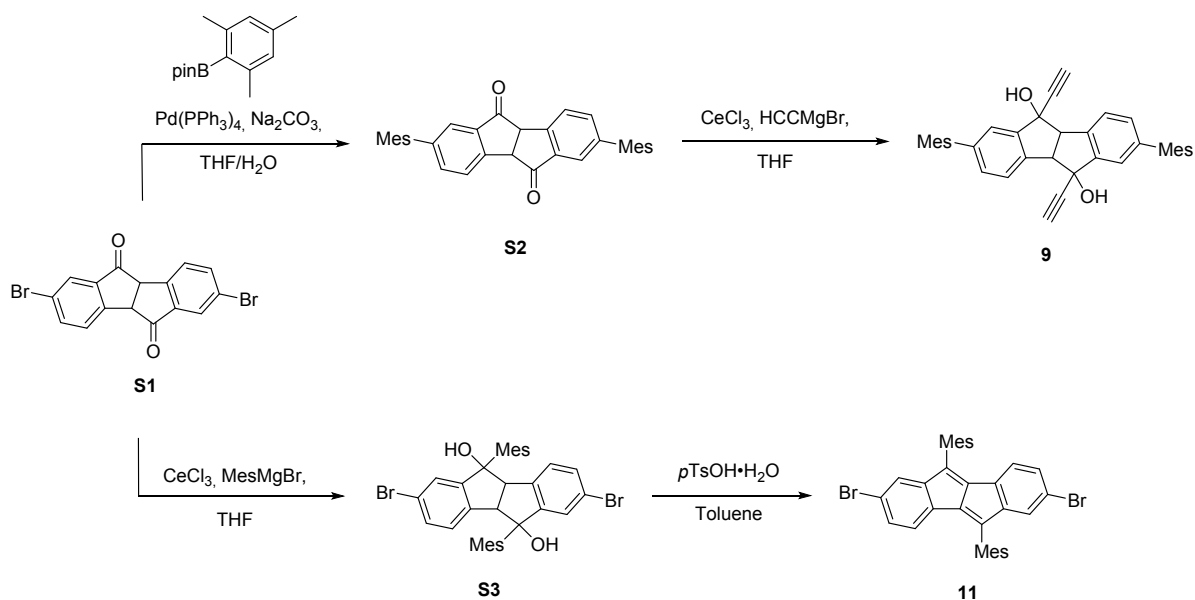
The measurement of cyclic voltammograms (CVs) was performed in solution and inside a glovebox using a METROHM Autolab PGSTAT 128N. As working electrode a GC (glassy carbon) electrode (2 mm diameters) was used. A platinum rod served as counter electrode, and as reference electrode a Ag/AgNO<sub>3</sub> electrode containing a silver wire immersed in an inner chamber filled with 0.1 M AgNO<sub>3</sub> containing 0.1 M *n*-Bu<sub>4</sub>NPF<sub>6</sub> in the outer chamber were used. For the internal reference, the ferrocene/ferrocenium (Fc/Fc<sup>+</sup>) redox couple was used.

## Absorption Spectroscopy

Absorption spectra were recorded on a SHIMADZU UV-1800 and were measured in a 10 mm fused quartz cuvette.

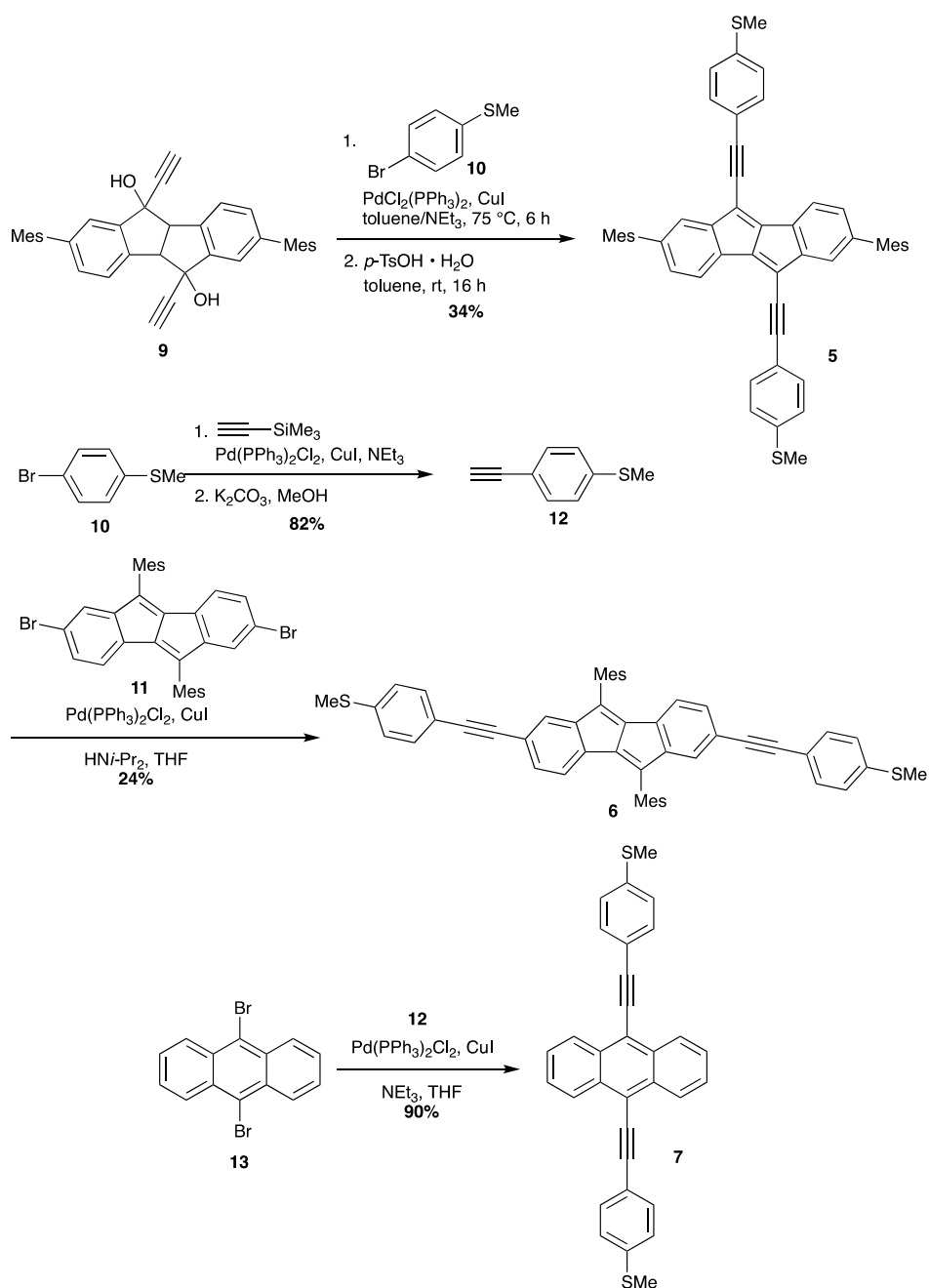
## 2 Synthetic Manipulations

The syntheses of diol **9**<sup>[3]</sup> and dibenzopentalene **11**<sup>[4]</sup> were carried out according to previously reported procedures starting from diketone **S1** (Scheme S1).



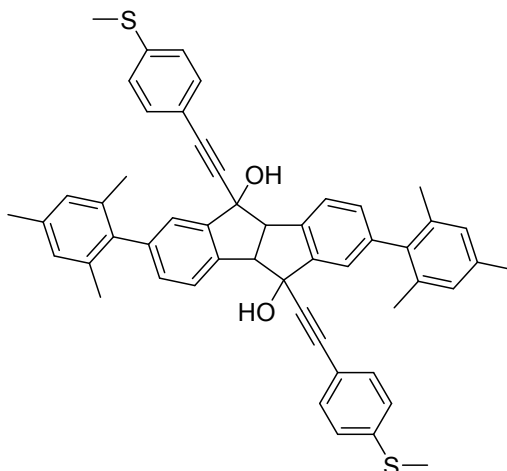
Scheme S1: Synthesis of the intermediates **9** and **11** starting from diketone **S1**.

The syntheses of **5**, **6** and **7** are shown in Scheme S2 and were carried out according to recently published procedures.<sup>31-34</sup> For target compound **5**, the synthesis proceeded from diol **9**.<sup>32</sup> A twofold Sonogashira reaction with *p*-bromo-thioanisole (**10**) followed by twofold water elimination under acidic conditions yielded **5**. **6** was accessible through a twofold Sonogashira reaction between bisbromide **11** and *p*-acetylene-thioanisole (**12**), which was previously synthesized from *p*-bromothioanisole (**10**).<sup>31,35</sup> The same procedure was applied for **7**, which was synthesized in a twofold Sonogashira reaction between 9,10-dibromoanthracene (**13**) and **12**.



Scheme S2: Synthesis of DBP derivatives **5**. And **6** and anthracene derivative **7**.

2.1 2,7-Dimesityl-5,10-bis((4-(methylthio)phenyl)ethynyl)-4b,5,9b,10-tetrahydroindeno[2,1-*a*]indene-5,10-diol (**S4**)

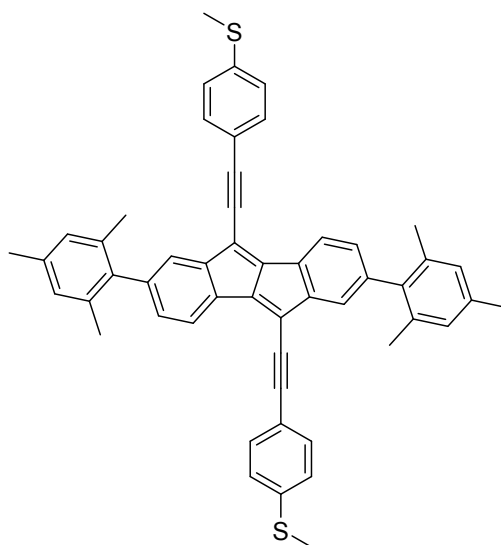


**S4**

Diol **9** (130 mg, 250  $\mu\text{mol}$ ),  $\text{PdCl}_2(\text{PPh}_3)_2$  (8.9 mg, 13  $\mu\text{mol}$ , 5 mol%), copper iodide (3.1 mg, 16  $\mu\text{mol}$ , 7 mol%) and 4-bromothioanisole (152 mg, 750  $\mu\text{mol}$ , 3 eq.) were dissolved in a mixture of anh. and degassed toluene (10 mL) and triethylamine (10 mL). The mixture was stirred at 90  $^\circ\text{C}$  for 48 h. After cooling to rt,  $\text{H}_2\text{O}$  (20 mL) was added. The organic layer was separated and the aq. layer was extracted with  $\text{CH}_2\text{Cl}_2$  (3  $\times$  30 mL). The combined organic layers were dried over  $\text{Na}_2\text{SO}_4$  and the solvent was removed under reduced pressure. The residue was purified by column chromatography ( $\text{SiO}_2$ , cyclohexane/EtOAc: 10/1 to 5/1) to obtain diol **S4** (56 mg, 108  $\mu\text{mol}$ , 30%) as an off-white solid.

$R_f$  0.33 (cyclohexane/EtOAc: 5/1);  $^1\text{H NMR}$  (400 MHz,  $\text{CDCl}_3$ , spectrum contains grease):  $\delta$  7.66 (dd,  $J = 7.8, 0.6$  Hz, 2H), 7.50 (dd,  $J = 1.5, 0.6$  Hz, 2H), 7.43–7.40 (m, 4H), 7.25 (dd,  $J = 7.7, 1.6$  Hz, 2H), 7.20–7.17 (m, 4H), 6.95 (s, 4H), 4.58 (s, 2H), 3.00 (s, 2H), 2.45 (s, 6H), 2.33 (s, 6H), 2.06 (s, 6H), 2.05 (s, 6H);  $^{13}\text{C NMR}$  (101 MHz,  $\text{CDCl}_3$ , spectrum contains grease):  $\delta$  148.5, 142.3, 140.0, 138.7, 136.9, 136.7, 136.4, 135.9, 132.3, 131.3, 128.4, 128.3, 126.2, 126.0, 125.8, 118.9, 90.3, 85.2, 75.8, 62.5, 21.2, 21.1, 21.0, 15.6; **HRMS** (ESI $^-$ ):  $m/z$  calcd. for  $\text{C}_{52}\text{H}_{46}\text{O}_2\text{ClS}_2$  801.2633 [M+Cl] $^-$ ; found 801.2631.

## 2.2 2,7-Dimesityl-5,10-bis((4-(methylthio)phenyl)ethynyl)indeno-[2,1-*a*]indene (**5**)

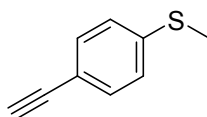


**5**

Diol **S4** (56 mg, 73  $\mu$ mol) was dissolved in toluene (10 mL) and *p*TsOH·H<sub>2</sub>O (7.1 mg, 37  $\mu$ mol, 0.5 eq) was added. The solution was stirred at rt for 16 h. H<sub>2</sub>O (20 mL) was added and the aq. layer was extracted with CH<sub>2</sub>Cl<sub>2</sub> (3  $\times$  30 mL). The combined organic layers were dried over Na<sub>2</sub>SO<sub>4</sub> and the solvent was removed under reduced pressure. The residue was purified by column chromatography (SiO<sub>2</sub>, cyclohexane/CH<sub>2</sub>Cl<sub>2</sub>: 5/1 to 3/1) to obtain DBP **5** (34 mg, 47  $\mu$ mol, 80%) as a dark red solid.

*R*<sub>f</sub> 0.41 (cyclohexane/CH<sub>2</sub>Cl<sub>2</sub>: 3/1); <sup>1</sup>H NMR (400 MHz, CDCl<sub>3</sub>):  $\delta$  7.48–7.45 (m, 4H), 7.42 (dd, *J* = 7.4, 0.6 Hz, 2H), 7.23–7.19 (m, 4H), 6.96 (s, 4H), 6.92 (dd, *J* = 1.5, 0.6 Hz, 2H), 6.78 (dd, *J* = 7.4, 1.5 Hz, 2H), 2.50 (s, 6H), 2.34 (s, 6H), 2.13 (s, 12H); <sup>13</sup>C NMR (101 MHz, CDCl<sub>3</sub>):  $\delta$  149.3, 148.9, 141.9, 141.1, 138.9, 136.9, 136.2, 132.4, 131.9, 128.9, 128.2, 125.9, 123.3, 122.6, 112.0, 119.0, 103.3, 84.8, 21.1, 20.8, 15.3; HRMS (APCI<sup>+</sup>): *m/z* calcd. for C<sub>52</sub>H<sub>43</sub>S<sub>2</sub> 731.2801 [M+H]<sup>+</sup>, found 731.2802.

### 2.3 4-Ethynylthioanisole (**12**)

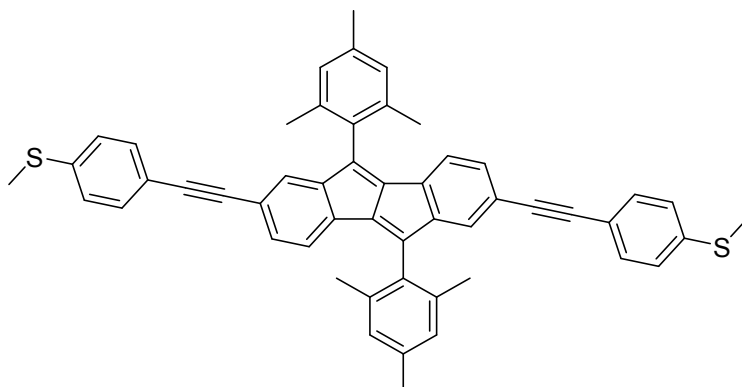


**12**

4-Bromothioanisole (**10**, 4.00 g, 19.7 mmol), Pd(PPh<sub>3</sub>)<sub>2</sub>Cl<sub>2</sub> (275 mg, 390 μmol, 2 mol%) and copper iodide (72 mg, 390 μmol, 2 mol%) were dissolved in anh. and degassed NEt<sub>3</sub> (50 mL) and trimethylsilylacetylene (3.64 mL, 2.52 g, 25.6 mmol, 1.3 eq.) was added. The mixture was stirred at 80 °C for 21 h. After cooling to rt, the solvent was removed under reduced pressure and the residue was purified by column chromatography (SiO<sub>2</sub>, cyclohexane/CH<sub>2</sub>Cl<sub>2</sub>: 1/0 to 0/1) to afford a yellowish liquid, which was dissolved in MeOH (40 mL). K<sub>2</sub>CO<sub>3</sub> (1.7 g, 12.4 mmol, 0.6 eq.) was added and the suspension was stirred at 40 °C for 15 h. The solvent was removed under reduced pressure and the residue was dissolved in CH<sub>2</sub>Cl<sub>2</sub> (50 mL) and H<sub>2</sub>O (50 mL). The organic layer was separated and the aq. layer was extracted with CH<sub>2</sub>Cl<sub>2</sub> (2 × 50 mL). The combined organic layers were washed with aq. sat. NaCl-solution (50 mL), dried over Na<sub>2</sub>SO<sub>4</sub> and the solvent was removed under reduced pressure to afford **12** (2.38 g, 16.2 mmol, 82%) as yellow-orange liquid.

The spectroscopic data matched those reported in the literature.<sup>[5]</sup>

## 2.4 2,7-Bis((4-(methylthio)phenyl)ethynyl)-5,10-dimesityl-5,10-indeno-[2,1-*a*]indene (**6**)

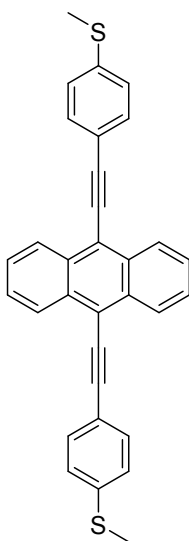


**6**

DBP **11** (100 mg, 168  $\mu\text{mol}$ ),  $\text{PdCl}_2(\text{PPh}_3)_2$  (12 mg, 17  $\mu\text{mol}$ , 10 mol%) and copper iodide (5 mg, 25  $\mu\text{mol}$ , 15 mol%) were dissolved in a mixture of anh. and degassed THF (10 mL) and (diisopropyl)amine (0.5 mL). 4-Ethynylthioanisole (**12**, 60 mg, 402  $\mu\text{mol}$ , 2.4 eq.) was added and the mixture was stirred at 65  $^\circ\text{C}$  for 26 h. After cooling to rt,  $\text{H}_2\text{O}$  (20 mL) was added. The organic layer was separated and the aq. layer was extracted with  $\text{CH}_2\text{Cl}_2$  (3  $\times$  30 mL). The combined organic layers were washed with  $\text{H}_2\text{O}$  (30 mL) and aq. sat. NaCl-solution, dried over  $\text{Na}_2\text{SO}_4$  and the solvent was removed under reduced pressure. The residue was purified by column chromatography ( $\text{SiO}_2$ , cyclohexane/EtOAc: 0/1 to 10/1) and subsequent washing with MeOH. **6** (29 mg, 40  $\mu\text{mol}$ , 24%) was afforded as a dark red solid.

$R_f$  0.69 (cyclohexane/EtOAc: 4/1);  $^1\text{H NMR}$  (500 MHz,  $\text{CDCl}_3$ ):  $\delta$  7.35–7.33 (m, 4H), 7.17–7.13 (m, 4H), 7.01 (s, 4H), 6.94 (dd,  $J = 7.6, 1.4$  Hz, 2H), 6.66 (d,  $J = 1.4$  Hz, 2H), 6.55 (dd,  $J = 7.6$  Hz, 2H), 2.47 (s, 6H), 2.38 (s, 6H), 2.29 (s, 12H);  $^{13}\text{C NMR}$  (126 MHz,  $\text{CDCl}_3$ ):  $\delta$  150.4, 144.6, 139.9, 139.1, 137.6, 136.2, 134.4, 131.7, 130.7, 129.1, 128.3, 125.7, 124.9, 122.6, 121.9, 119.4, 89.9, 89.6, 21.1, 20.1, 15.3; **HRMS** (APCI $^+$ ):  $m/z$  calcd. for  $\text{C}_{53}\text{H}_{47}\text{OS}_2$  763.3063  $[\text{M}+\text{MeOH}+\text{H}]^+$ , found 763.3064.

## 2.5 9,10-Bis((4-(methylthio)phenyl)ethynyl)anthracene (**7**)



**7**

9,10-Dibromoanthracene (348 mg, 1.00 mmol), 4-ethynylthioanisole (**12**, 327 mg, 2.20 mmol, 2.2 eq), PdCl<sub>2</sub>(PPh<sub>3</sub>)<sub>2</sub> (57 mg, 8.0 μmol, 8 mol%) and copper iodide (30 mg, 15 μmol, 15 mol%) were dissolved in a mixture of anh. and degassed toluene (15 mL) and triethylamine (15 mL). The mixture was stirred at 65 °C for 48 h. After cooling to rt the solvent was removed under reduced pressure and the residue was suspended in MeOH (25 mL). The solid was filtered and recrystallized from CHCl<sub>3</sub> to obtain **7** (420 mg, 893 μmol, 90%) as orange-brown solid, which is highly yellow-greenish fluorescent in solution.

<sup>1</sup>H NMR (400 MHz, CDCl<sub>3</sub>): δ 8.70–8.66 (m, 4H), 7.70–7.67 (m, 4H), 7.67–7.62 (m, 4H), 7.33–7.30 (m, 4H), 2.56 (s, 6H); <sup>13</sup>C NMR (101 MHz, CDCl<sub>3</sub>): δ 140.1, 132.1, 132.0, 127.4, 126.9, 126.1, 119.8, 118.5, 102.4, 86.8, 15.5.; HRMS (ESI<sup>+</sup>): *m/z* calcd. for C<sub>32</sub>H<sub>22</sub>S<sub>2</sub> 470.1157 [M]<sup>+</sup>, found 470.1159.

### 3 NMR spectra

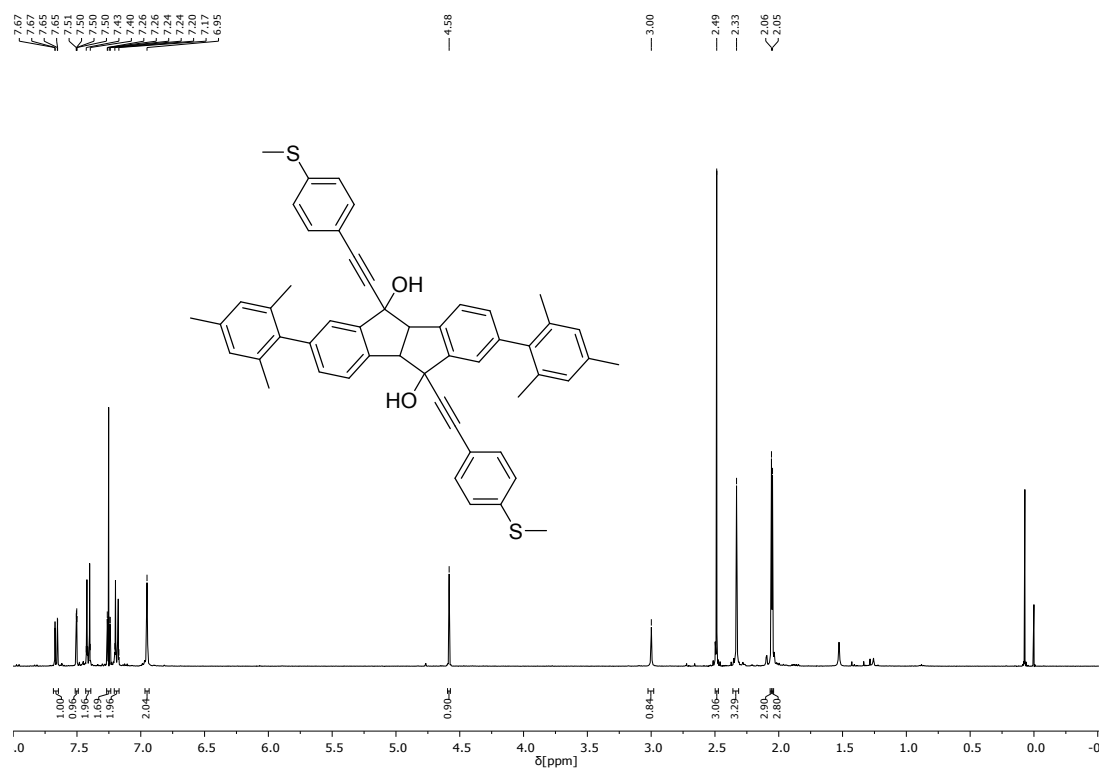


Figure S1: <sup>1</sup>H NMR-spectrum of 2,7-Dimesityl-5,10-bis((4-(methylthio)phenyl)ethynyl)-4b,5,9b,10-tetrahydroindeno[2,1-a]indene-5,10-diol (**S4**) in CDCl<sub>3</sub> (400 MHz).

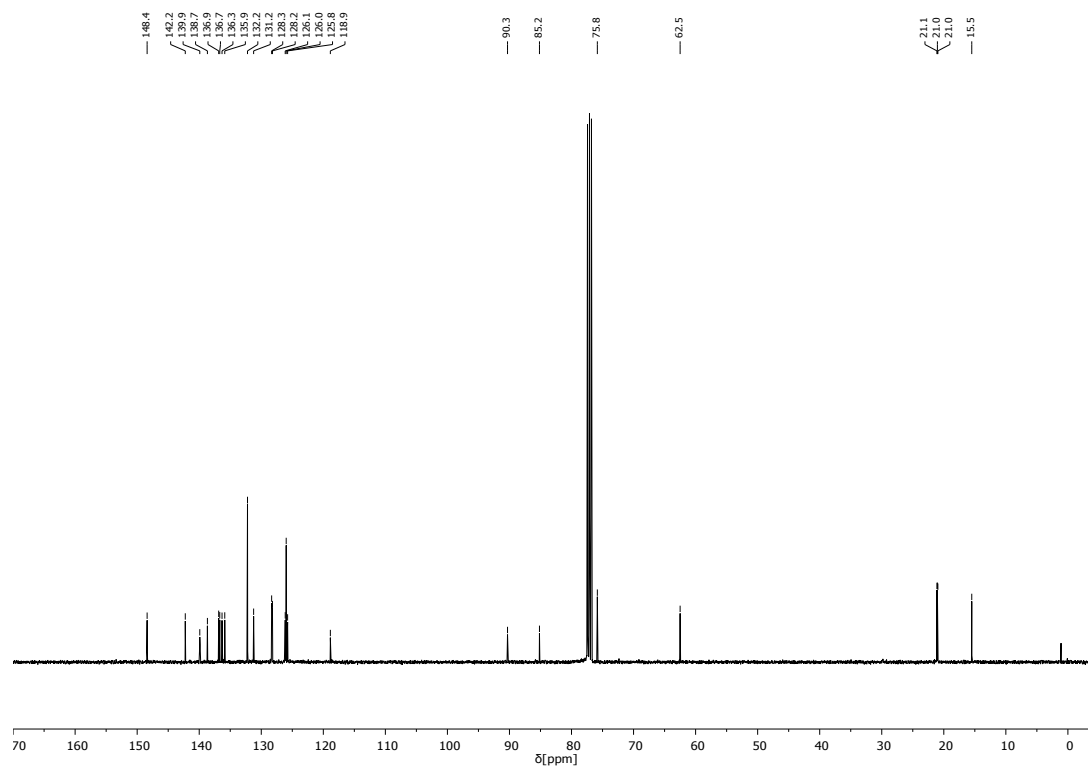


Figure S2: <sup>13</sup>C NMR-spectrum of 2,7-Dimesityl-5,10-bis((4-(methylthio)phenyl)ethynyl)-4b,5,9b,10-tetrahydroindeno[2,1-a]indene-5,10-diol (**S4**) in CDCl<sub>3</sub> (101 MHz).

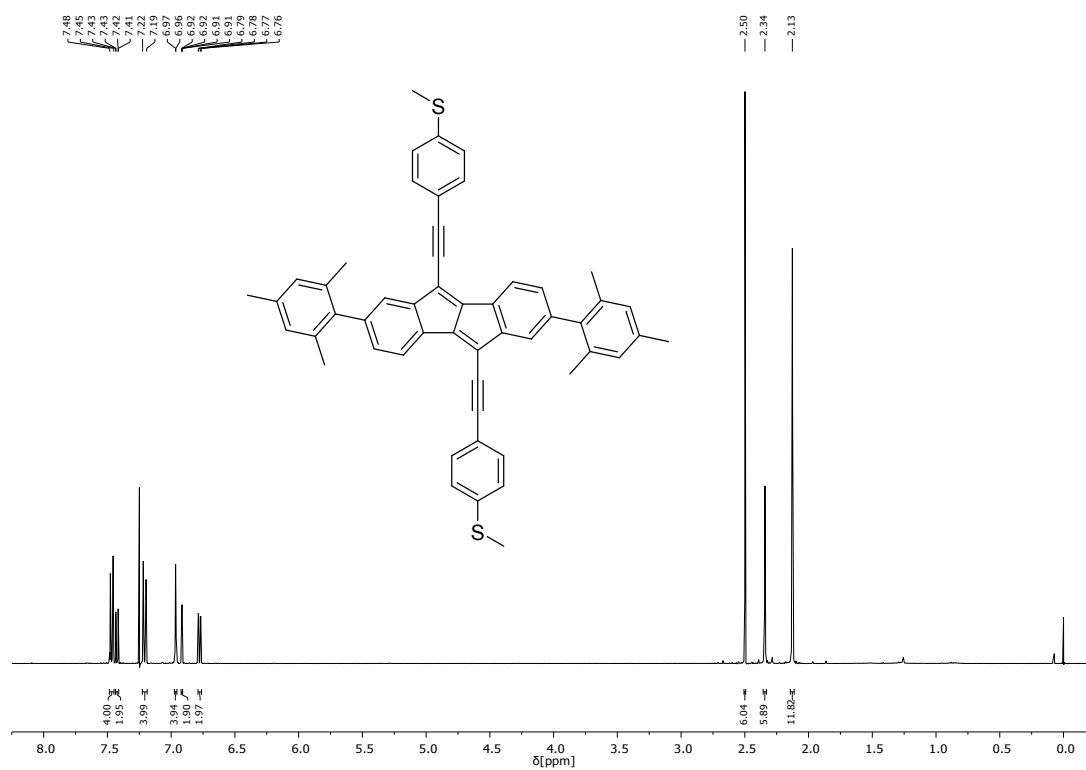


Figure S3: <sup>1</sup>H NMR-spectrum of 2,7-Dimesityl-5,10-bis((4-(methylthio)phenyl)ethynyl)indeno-[2,1-a]indene (5) in CDCl<sub>3</sub> (400 MHz).

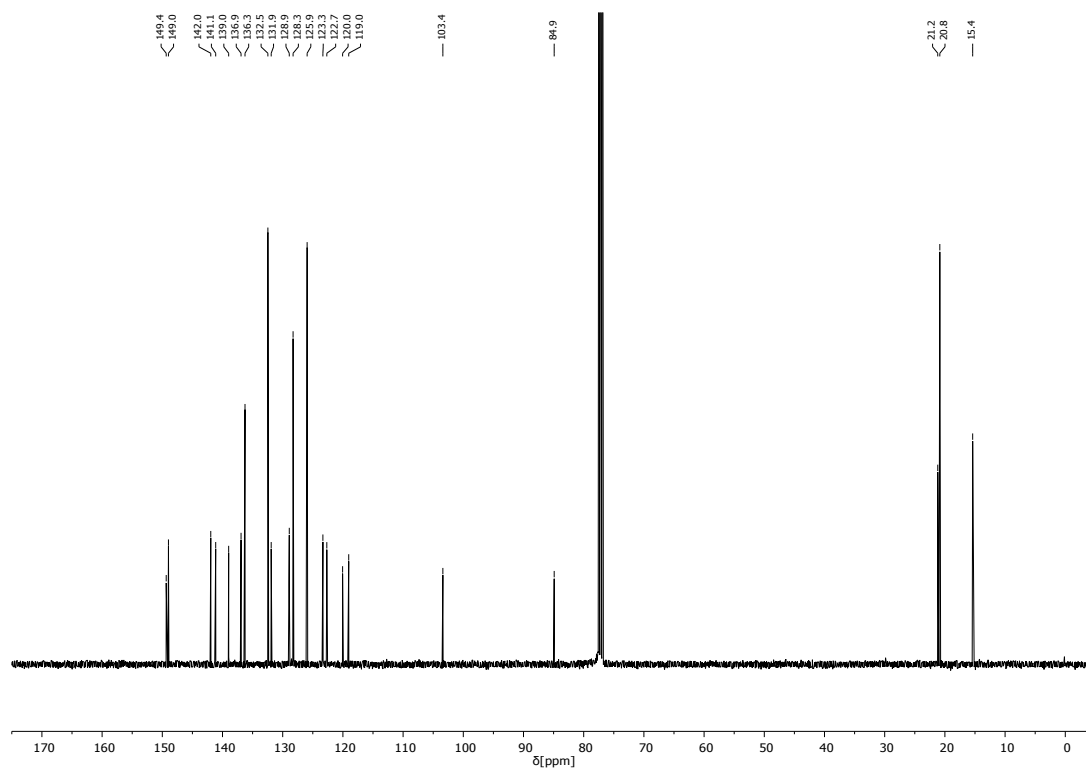


Figure S4: <sup>13</sup>C NMR-spectrum of 2,7-Dimesityl-5,10-bis((4-(methylthio)phenyl)ethynyl)indeno-[2,1-a]indene (5) in CDCl<sub>3</sub> (101 MHz).

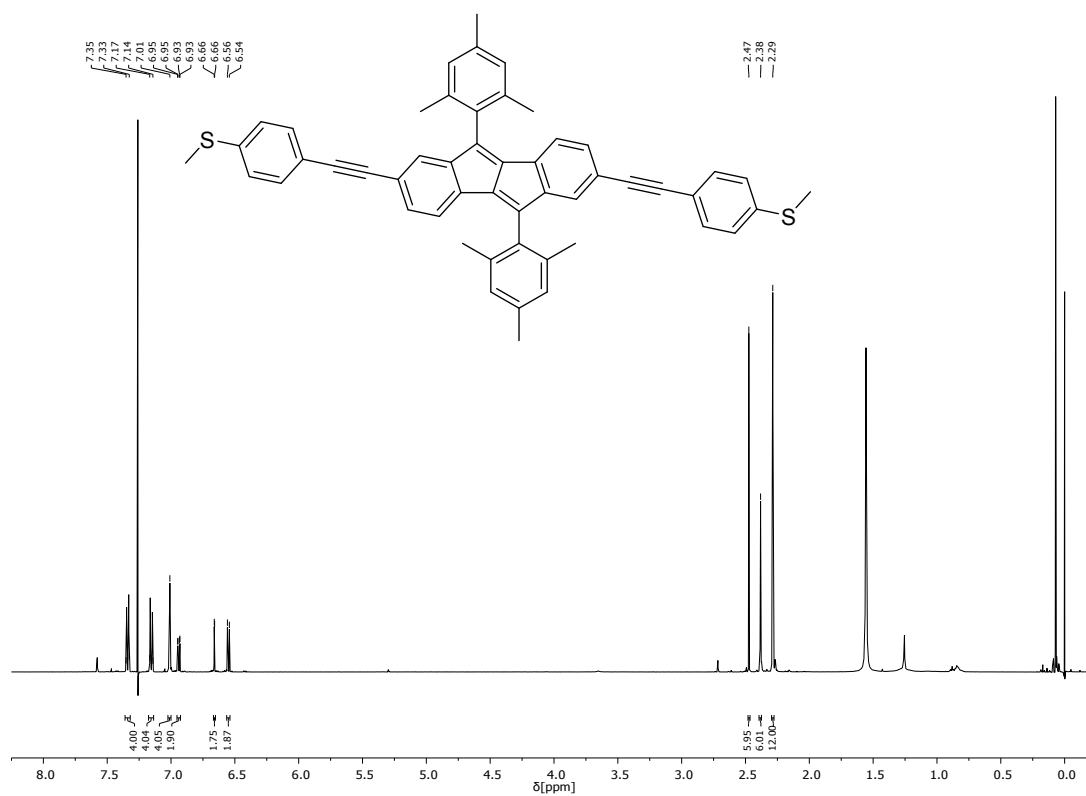


Figure S5:  $^1\text{H}$  NMR-spectrum of 2,7-bis((4-(methylthio)phenyl)ethynyl)-5,10-dimesityl-5,10-indeno-[2,1-a]indene (**6**) in  $\text{CDCl}_3$  (500 MHz).

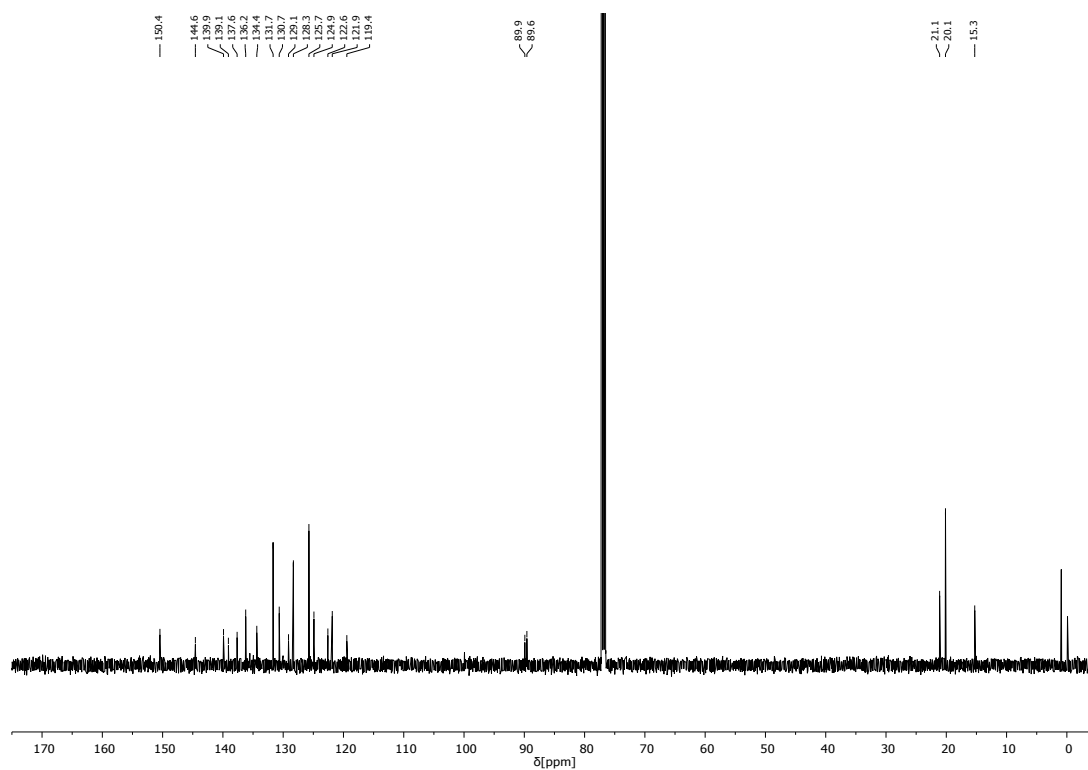


Figure S6:  $^{13}\text{C}$  NMR-spectrum of 2,7-bis((4-(methylthio)phenyl)ethynyl)-5,10-dimesityl-5,10-indeno-[2,1-a]indene (**6**) in  $\text{CDCl}_3$  (101 MHz).

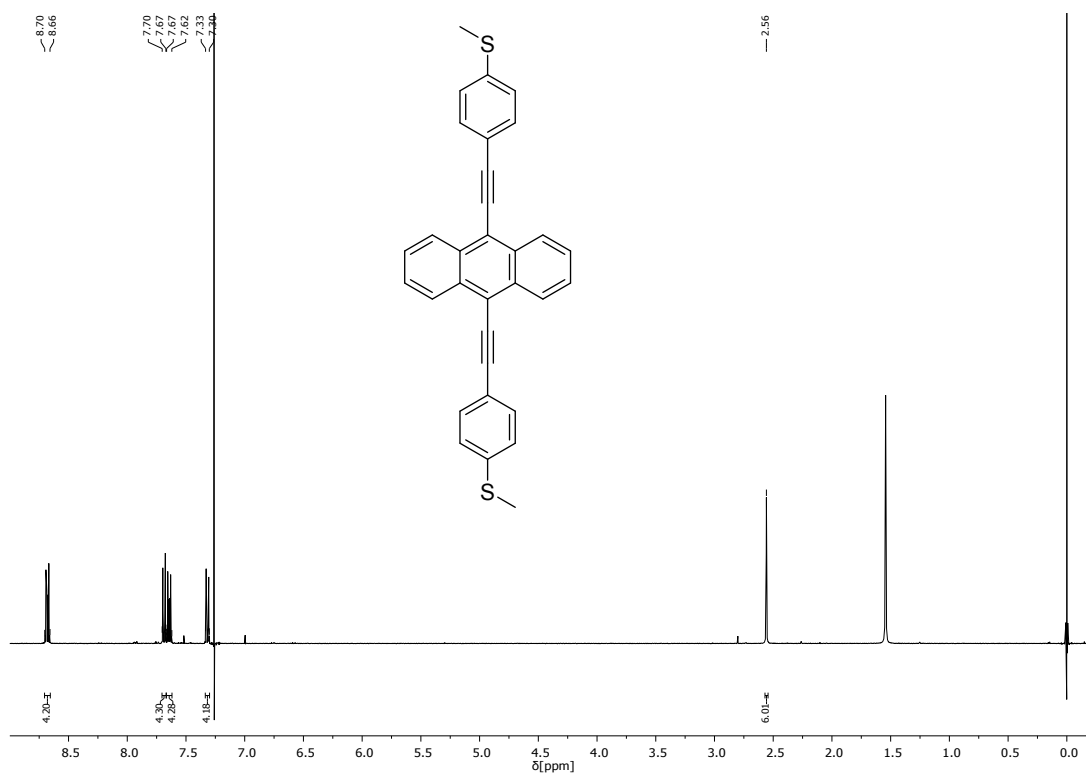


Figure S7: <sup>1</sup>H NMR-spectrum of 9,10-bis((4-(methylthio)phenyl)ethynyl)anthracene (**7**) in CDCl<sub>3</sub> (400 MHz).

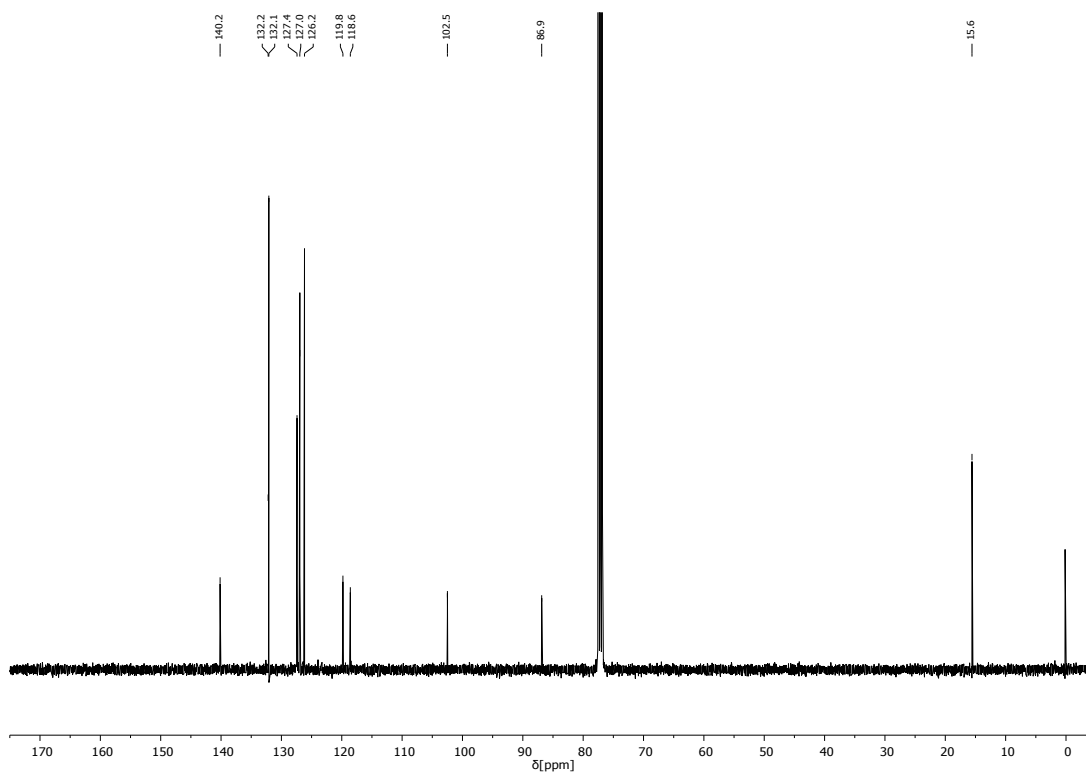


Figure S8: <sup>13</sup>C NMR-spectrum of 9,10-bis((4-(methylthio)phenyl)ethynyl)anthracene (**7**) in CDCl<sub>3</sub> (101 MHz).

## 4 Absorption Spectra

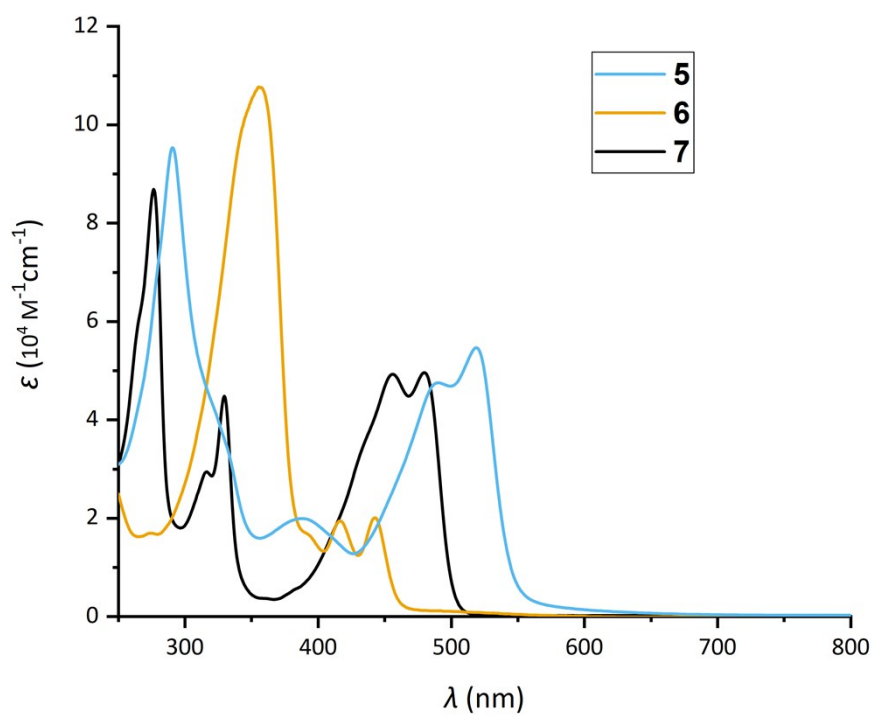


Figure S9: Absorption spectra of **5** (blue), **6** (yellow) and **7** (black) in  $\text{CH}_2\text{Cl}_2$ .

## 5 Cyclic Voltammograms

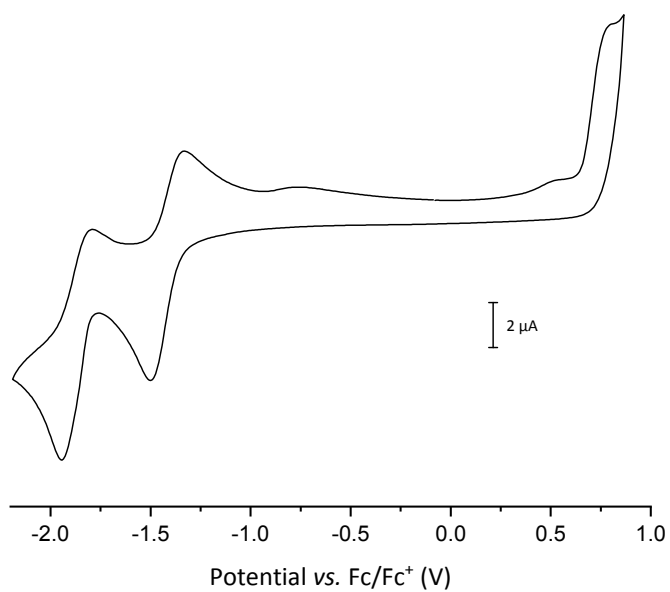


Figure S10: Cyclic voltammogram of **5** (1 mM in  $\text{CH}_2\text{Cl}_2$ , 0.1 M  $n\text{-Bu}_4\text{NPF}_6$ , glassy carbon electrode, scan rate  $0.1 \text{ V s}^{-1}$ ).

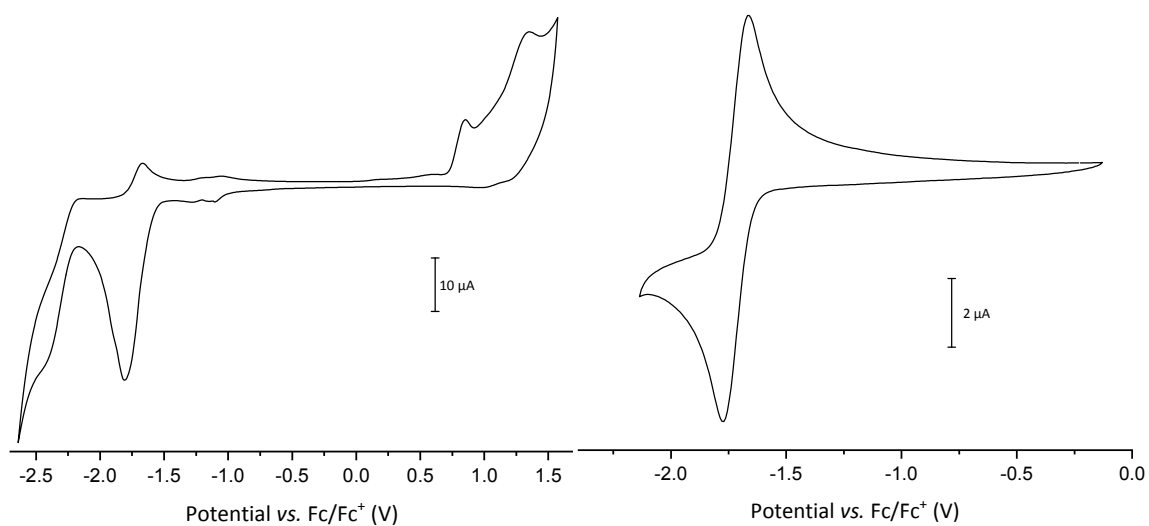


Figure S11: Cyclic voltammograms of **6** (1 mM in  $\text{CH}_2\text{Cl}_2$ , 0.1 M  $n\text{-Bu}_4\text{NPF}_6$ , glassy carbon electrode, scan rate  $0.1 \text{ V s}^{-1}$ ).

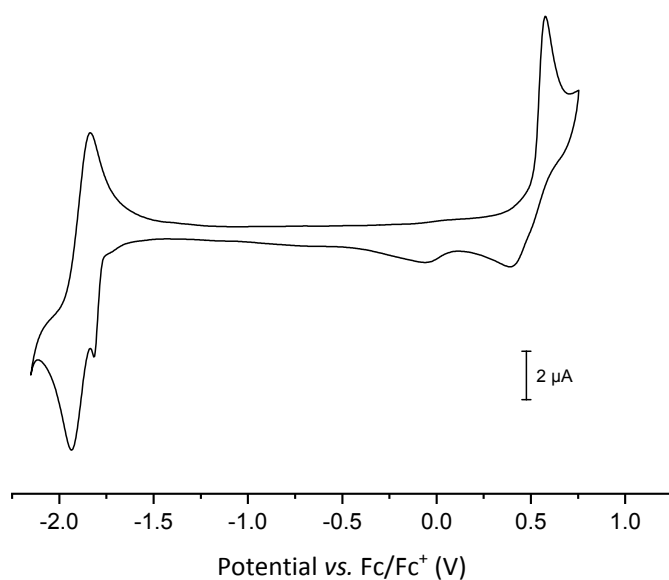


Figure S12: Cyclic voltammogram of **7** (1 mM in  $\text{CH}_2\text{Cl}_2$ , 0.1 M  $n\text{-Bu}_4\text{NPF}_6$ , glassy carbon electrode, scan rate  $0.1 \text{ V s}^{-1}$ ).

## 6 DFT calculations

DFT calculations were performed with either the TURBOMOLE v7.3.1 program package<sup>[6]</sup> or the Gaussian 16 program package.<sup>[7]</sup> The resolution-of-identity<sup>[8]</sup> (RI) approximation for the Coulomb integrals was used in all DFT calculations. Further, the D3 dispersion correction scheme<sup>[9,10]</sup> with the Becke-Johnson damping function was applied.<sup>[11,12]</sup> Using TURBOMOLE, the geometries of all molecules were optimized without symmetry restrictions with the PBEh-3c<sup>[13]</sup> composite scheme followed by harmonic vibrational frequency analyses to confirm minima as stationary points. NICS values were calculated using the GIAO (Gauge Including Atomic Orbital)<sup>[14]</sup> method at the B3LYP/6-31G\*<sup>[15]</sup> level of theory.

### 6.1 NICS(1)<sub>iso</sub>-calculations

Nucleus independent chemical shifts (NICS)<sup>[16,17]</sup> were calculated using the Gaussian 16 program package applying the standard Gauge-including Atomic Orbitals (GIAO) method on the B3LYP/6-31G(d) level of theory. Negative NICS values indicate a diatropic ring current (associated with an aromatic character) while positive NICS values indicate a paratropic ring current (associated with an antiaromatic character). Dummy atoms (Bq) were placed in the center of atoms of each ring 1 Å above the respective ring plane (as shown below), and the NICS values were averaged for each ring size.

Table S1: NICS(1)<sub>iso</sub> values for **5–7**.

	5-membered rings	6-membered rings
<b>5</b>	5.3	-6.9
<b>6</b>	4.6	-6.7
	inner ring	outer rings
<b>7</b>	-12.7	-11.4

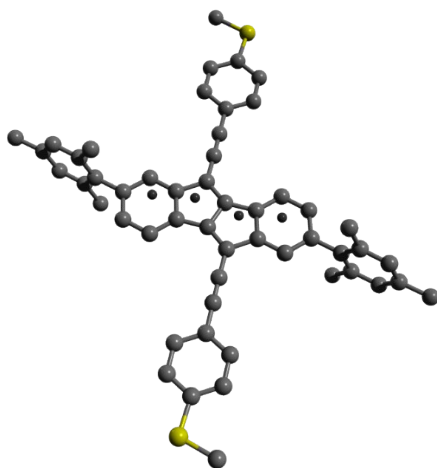


Figure S13: Representative positions of the atoms for NICS(1)<sub>iso</sub> calculations for **5**. Each dummy atom is positioned 1 Å above the respective ring plane.

## 7 Summary of electrochemical and optical properties

	$E_{1/2,Red}$ (V) <sup>[a]</sup>	$E_{Ox}$ (V) <sup>[a]</sup>	LUMO <sub>CV</sub> (eV) <sup>[b]</sup>	HOMO <sub>CV</sub> (eV) <sup>[b]</sup>	$E_{g, CV}$ (eV)	$E_{g, opt}$ (eV) <sup>[c]</sup>	LUMO <sub>calc</sub> (eV) <sup>[d]</sup>	HOMO <sub>calc</sub> (eV) <sup>[d]</sup>	$E_{g, calc}$ (eV)
<b>5</b>	-1.87 -1.42	0.80	-3.46	-5.45	1.99	1.73	-2.80	-5.23	2.43
<b>6</b>	-1.74	0.85	-3.15	-5.51	2.36	2.06	-2.52	-5.14	2.62
<b>7</b>	-1.89	0.58	-3.02	-5.31	2.29	2.48	-2.39	-4.97	2.58

[a] measured in CH<sub>2</sub>Cl<sub>2</sub> vs. ferrocene. [b] From the onsets of the first reduction/oxidation peaks, assuming an ionization energy of 4.8 eV for ferrocene.<sup>[18]</sup> [c] Optical band gap from the onsets of the longest wavelength absorption band. [d] B3LYP-D3/def2-TZVP.

## 8 Single Crystal X-Ray Diffraction

Single crystals for **5** and **6** were obtained by layering a CH<sub>2</sub>Cl<sub>2</sub> solution with MeOH. A single crystal for **7** was obtained by recrystallization from hot toluene. The data were collected from a shock-cooled single crystal at 100(2) K on a BRUKER APEX2 QUAZAR three-circle diffractometer with a microfocus sealed X-ray tube using mirror optics as monochromator and a Bruker APEXII detector. The diffractometer was equipped with an Oxford Cryostream 800 low temperature device and used MoK<sub>α</sub> radiation ( $\lambda = 0.71073 \text{ \AA}$ ). All data were integrated with SAINT<sup>[19]</sup> and a multi-scan absorption correction using SADABS<sup>[20]</sup> was applied. The structures were solved by direct methods using SHELXT 2014/5<sup>[21]</sup> and refined by full-matrix least-squares methods against  $F^2$  by SHELXL 2018/3<sup>[22]</sup> using ShelXle (Rev 1046)<sup>[23]</sup>. All non-hydrogen atoms were refined with anisotropic displacement parameters. The hydrogen atoms were refined isotropically on calculated positions using a riding model with their  $U_{\text{iso}}$  values constrained to 1.5 times the  $U_{\text{eq}}$  of their pivot atoms for terminal sp<sup>3</sup> carbon atoms and 1.2 times for all other carbon atoms. Crystallographic data (including structure factors) for the structures reported in this paper have been deposited with the Cambridge Crystallographic Data Centre and can be obtained free of charge via [www.ccdc.cam.ac.uk/structures](http://www.ccdc.cam.ac.uk/structures).

The structure of **7** was identified as a pseudo-merohedral twin with the twin law  $(-1\ 0\ 0)\ (0\ -1\ 0)\ (0\ 0\ 1)$  and solved in the space group P-1.

The crystal of **6** diffracted weakly and only a resolution of 1.0 Å could be reached. The data collected is sufficient for a proof of structure and molecule length excluding bond lengths.

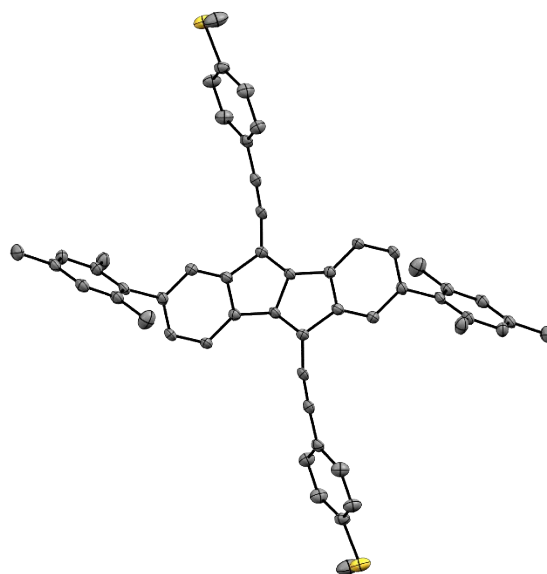


Figure S14: Molecular structure of **5** in the solid state (displacement ellipsoids are shown at the 50% probability level; hydrogen atoms are omitted for clarity).

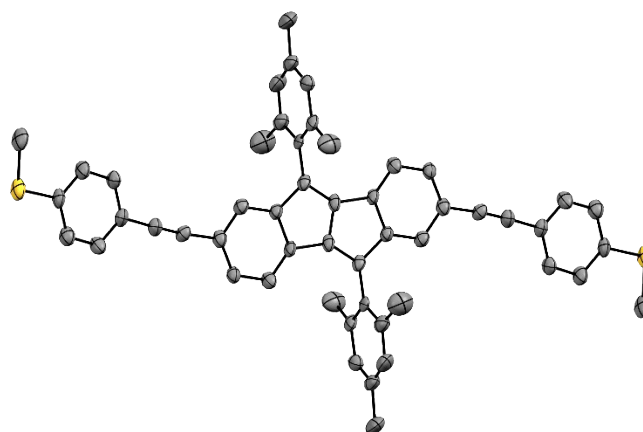


Figure S15: Molecular structure of **6** in the solid state (displacement ellipsoids are shown at the 50% probability level; hydrogen atoms are omitted for clarity).

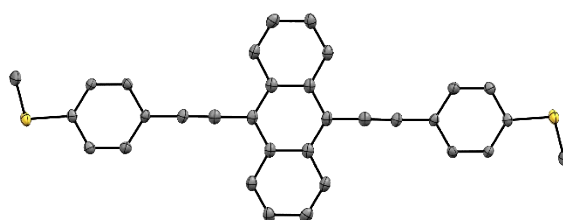


Figure S16: Molecular structure of **7** in the solid state (displacement ellipsoids are shown at the 50% probability level; hydrogen atoms are omitted for clarity).

Table S2: Crystal data and refinement parameters for **5**, **6** and **7**.

Compound	<b>5</b>	<b>6</b>	<b>7</b>
CCDC number	1977533	1982996	1983044
Empirical formula	C <sub>52</sub> H <sub>42</sub> S <sub>2</sub>	C <sub>52</sub> H <sub>42</sub> S <sub>2</sub>	C <sub>32</sub> H <sub>22</sub> S <sub>2</sub>
Formula weight	730.97	730.97	470.61
Temperature [K]	100(2)	100(2)	100(2)
Crystal system	triclinic	monoclinic	triclinic
Space group (number)	$P\bar{1}$ (2)	$P2_1/c$ (14)	$P\bar{1}$ (2)
<i>a</i> [Å]	8.334(11)	10.284(16)	5.323(4)
<i>b</i> [Å]	10.560(13)	7.894(17)	7.924(6)
<i>c</i> [Å]	12.426(14)	24.43(4)	28.58(2)
$\alpha$ [Å]	90.25(2)	90	89.815(13)
$\beta$ [Å]	107.99(2)	99.52(2)	89.07(3)
$\gamma$ [Å]	107.34(3)	90	89.71(2)
Volume [Å <sup>3</sup> ]	987(2)	1956(6)	1205.1(15)
<i>Z</i>	1	2	2
$\rho_{\text{calc}}$ [g/cm <sup>3</sup> ]	1.230	1.241	1.297
$\mu$ [mm <sup>-1</sup> ]	0.171	0.173	0.240
<i>F</i> (000)	386	772	492
Crystal size [mm <sup>3</sup> ]	0.120×0.100×0.040	0.300×0.080×0.030	0.400×0.040×0.020
Crystal colour	red	red	orange
Crystal shape	block	plate	needle
Radiation	MoK $\alpha$ ( $\lambda$ =0.71073 Å)	MoK $\alpha$ ( $\lambda$ =0.71073 Å)	MoK $\alpha$ ( $\lambda$ =0.71073 Å)
2 $\theta$ range [°]	3.47 to 55.03 (0.77 Å)	3.38 to 42.15 (0.99 Å)	1.43 to 55.31 (0.77 Å)
Index ranges	-10 ≤ <i>h</i> ≤ 10 -13 ≤ <i>k</i> ≤ 13 -16 ≤ <i>l</i> ≤ 16	-10 ≤ <i>h</i> ≤ 10 -7 ≤ <i>k</i> ≤ 7 -24 ≤ <i>l</i> ≤ 24	-6 ≤ <i>h</i> ≤ 6 -10 ≤ <i>k</i> ≤ 10 -37 ≤ <i>l</i> ≤ 36
Reflections collected	15957	20182	22148
Independent reflections	4530 $R_{\text{int}} = 0.0941$ $R_{\text{sigma}} = 0.0854$	2102 $R_{\text{int}} = 0.1567$ $R_{\text{sigma}} = 0.0961$	5540 $R_{\text{int}} = 0.0943$ $R_{\text{sigma}} = 0.0906$
Completeness to $\theta = 25.242^\circ$	100.0 %	99.2 %*	100.0 %
Data / Restraints / Parameters	4530/0/248	2102/200/248	5540/214/310
Goodness-of-fit on $F^2$	1.034	1.100	1.079
Final <i>R</i> indexes [ $I \geq 2\sigma(I)$ ]	$R_1 = 0.0589$ $wR_2 = 0.1375$	$R_1 = 0.0929$ $wR_2 = 0.2077$	$R_1 = 0.0746$ $wR_2 = 0.1886$
Final <i>R</i> indexes [all data]	$R_1 = 0.1011$ $wR_2 = 0.1585$	$R_1 = 0.1364$ $wR_2 = 0.2348$	$R_1 = 0.0993$ $wR_2 = 0.2045$
Largest peak/hole [eÅ <sup>3</sup> ]	0.47/-0.36	0.55/-0.32	0.83/-1.29

\*Completeness to  $\theta = 21.075^\circ$

## 9 STM Breakjunction Measurements

### 9.1 Sample preparation for single-molecule experiments.

Each compound was deposited onto a freshly flame-annealed gold substrate from a 0.1–1.0 mM dichloromethane solution, using an immersion time of 5–10 minutes. After this time, the substrate was removed and blown dry under N<sub>2</sub>. To prepare the tip we mechanically cut a gold wire, rinsed it with ethanol and then passed it briefly through a butane flame prior to mounting.

### 9.2 Single-Molecule Conductivity Studies.

The conductance of each compound was measured using the STM-BJ method. All experiments were performed using a home-built STM, optimized for measurements under ambient conditions. During the break-junction experiment, the tip is moved vertically in and out of contact with the substrate at a constant speed of approximately 10 nm/s, in 1 pm steps. For the conductance ( $G = I/V$ ) versus distance measurements, a bias voltage  $V$  of 0.2 V was applied between the tip and the substrate. A linear current-to-voltage converter with two amplification stages allows us to record conductance values over a large dynamic range. The gains used in this study were  $4.4 \times 10^7 \text{ VA}^{-1}$  and  $2.1 \times 10^9 \text{ VA}^{-1}$  for compounds **5**, **7** and **8**. We also place a resistor in series with the circuit of 1 M $\Omega$ . For compound **6** we used gains of  $5 \times 10^8 \text{ VA}^{-1}$  and  $2.4 \times 10^{10} \text{ VA}^{-1}$  and a 12 M $\Omega$  series resistor.

The motion of the tip and the conductance measurement are controlled by an in-house computer program to record conductance versus tip-displacement ( $G$  vs.  $z$ ) curves. Typically, when moving out of contact, we move several nm after reaching our lower conductance limit. When in contact, the piezo moves a further 1–2 nm after reaching  $1.0 G_0$ . These limits guarantee that a broad gold contact is formed and broken in each cycle, and that any molecular junction is broken at the end of the cycle. We aim to carry out 5000–10000 approach and retraction cycles in each run, and we vary the location of the tip over the sample in order to avoid systematic errors in the data. We focus on the opening stages of the cycle. After data acquisition is complete, we first remove any blocks of traces in which there is a clear degradation in trace quality due (most likely) to tip blunting or excessive build-up of material between the electrodes. We then use an automated routine to separate traces displaying

plateaus from those with tunnelling-only. This searches for regions of individual traces in which the conductance change is less than a certain amount across a minimum distance interval (for example, a plateau is identified when a  $\Delta z > 0.1$  nm is needed to produce a change in conductance of  $\Delta \log(G/G_0) < 0.1$  at any region below  $0.5 G_0$ ). We aim to use very similar criteria for all compounds. We divide each measurement for a molecule into blocks of 500 sequential traces and reject any set for which the overall percentage of traces with plateaus exceeds 50%. This avoids having a significant contribution of multi-molecular junctions in the final histogram.

After generating the 1D histograms, we obtain the single molecule conductance for each compound by fitting a single gaussian to the peak in the corresponding 1D histogram. The histograms were normalised according to the procedure previously described.<sup>30</sup> To calculate the plateau lengths for each individual  $G(z)$  trace, we measure the distance between two points in each trace, just after the Au-Au junction cleavage ( $\log(G/G_0) = -0.5$ ) to the last point in the trace which occurs one order of magnitude below the main conductance (determined from the 1D histogram peak). Finally, we add 0.4 nm to account for the initial jump-out-of-contact (please see SI Figure S26 for further details). Each individual length is then plotted in a histogram to show the total distribution.

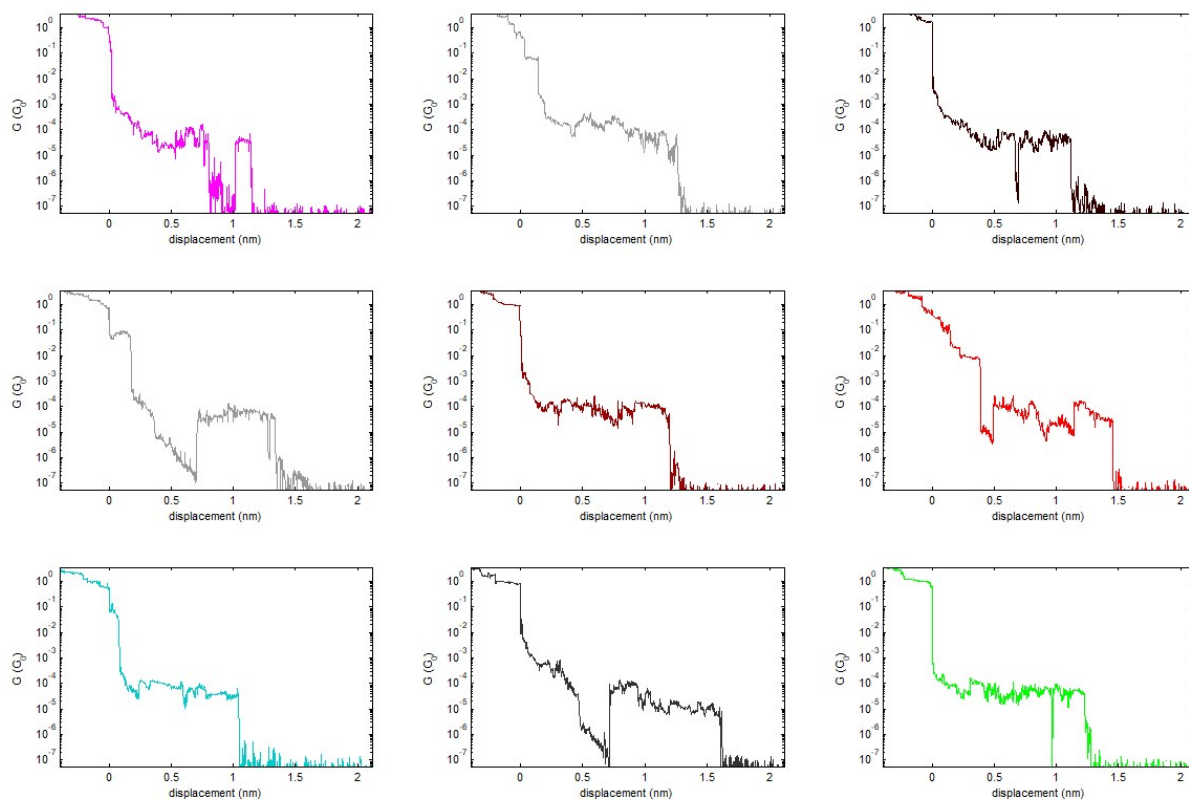


Figure S17. Examples of individual molecular-junctions for compound 5.

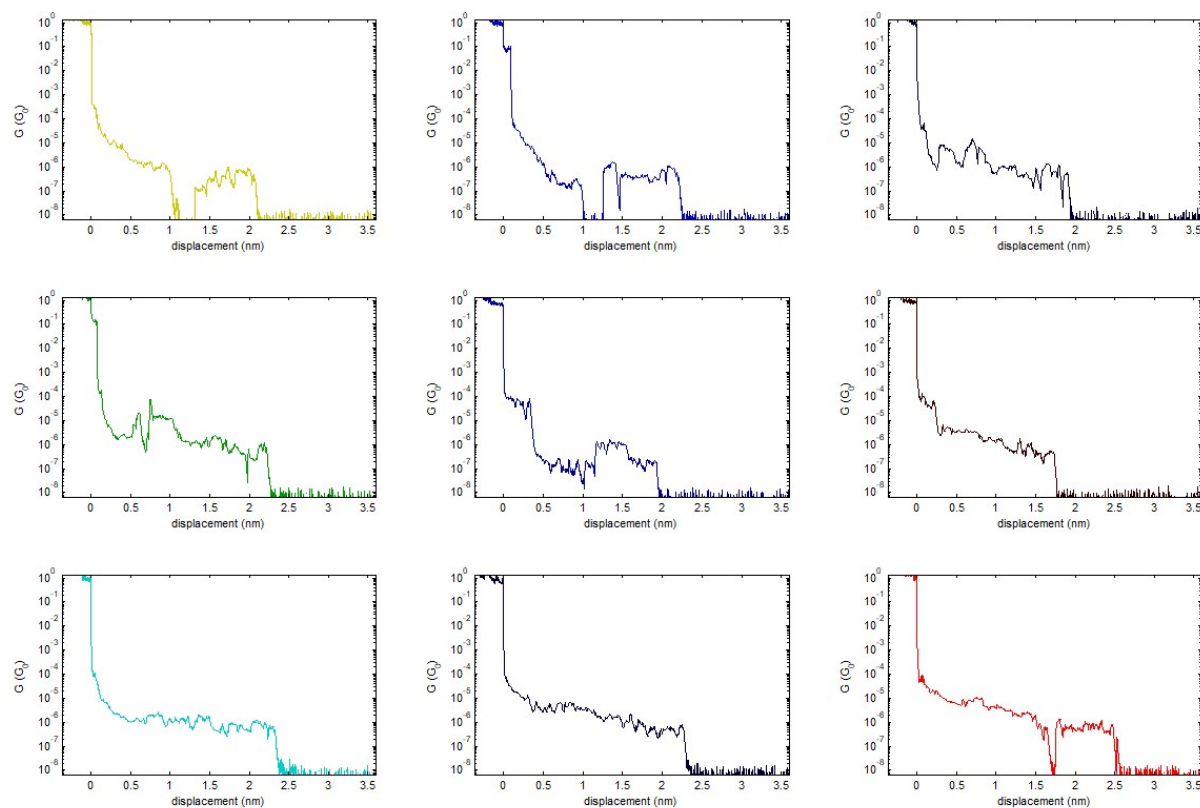


Figure S18. Examples of individual molecular-junctions for compound 6.

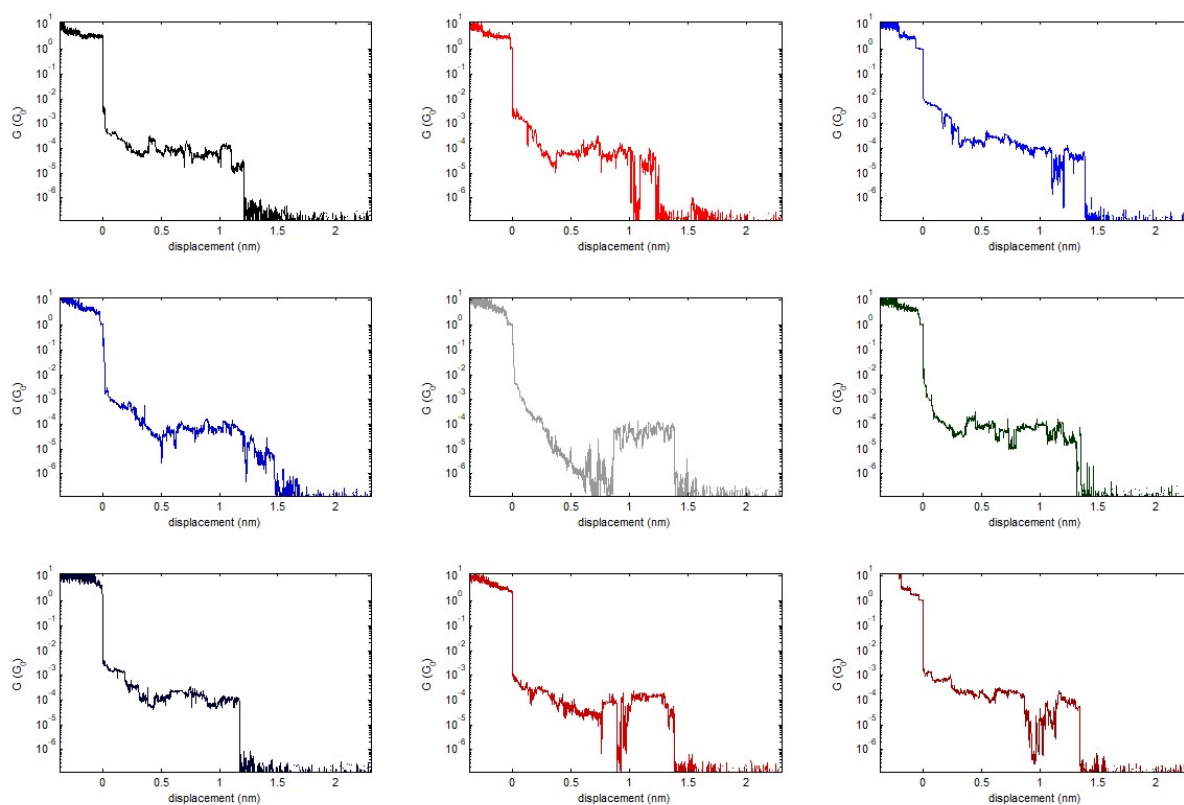


Figure S19. Examples of individual molecular-junctions for compound **7**.

### 9.3 Conductance versus voltage behaviour

To record I-V curves, we pause the piezo movement at defined points during the stretching of a single junction and perform a voltage ramp. This is done at set intervals (usually every 0.5 to 1 Å) during an opening trace (the precise number of I-V curves recorded depends on the length of the plateau). We aim to record several hundred molecular junctions. Between each cycle (starting at +V, ramping to -V and then back to +V) we return the voltage to the preset value (+0.2 V) and continue recording the current as the piezo is moved, thus allowing us to build a G(z) trace to monitor the evolution of the junction in detail. To normalize the G-V curves, we divide the entire trace by the conductance at low bias.

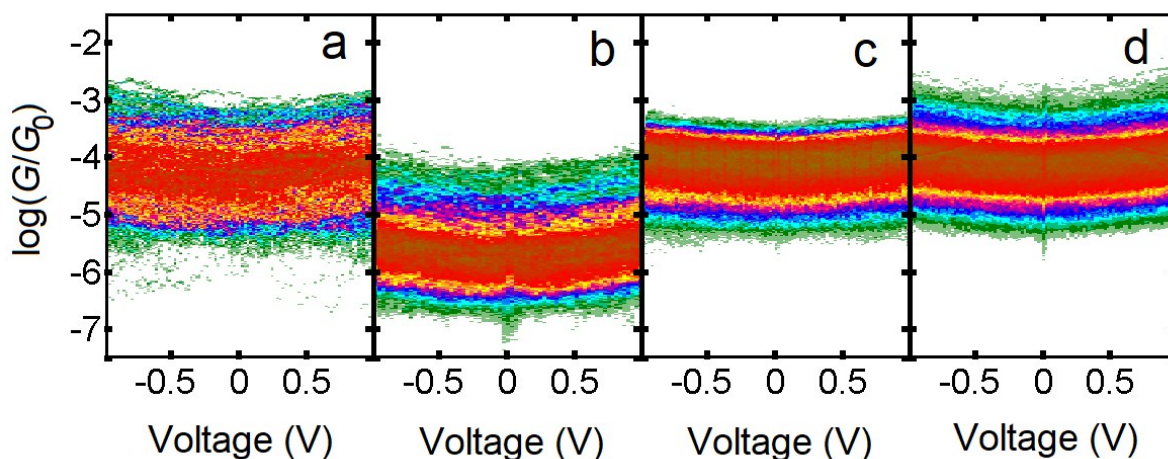


Figure S20. 2D histograms of all  $G$ - $V$  traces recorded for junctions of: a) **5**. b) **6**. c) **7**. d) **8**. The range measured for **6** and **8** was  $\pm 1.0$  V,  $\pm 1.5$  V for **5** and  $\pm 1.6$  V for **7** (only shown up to  $\pm 1.0$  V in this figure). The number of junctions and  $G$ - $V$  traces included is the following: Compound **5**: 262  $G$ - $V$  curves from 223 junctions. Compound **6**: 912  $G$ - $V$  curves from 93 junctions. Compound **7**: 291  $G$ - $V$  curves from 428 junctions. Compound **8**: 3368  $G$ - $V$  curves from 101 junctions.

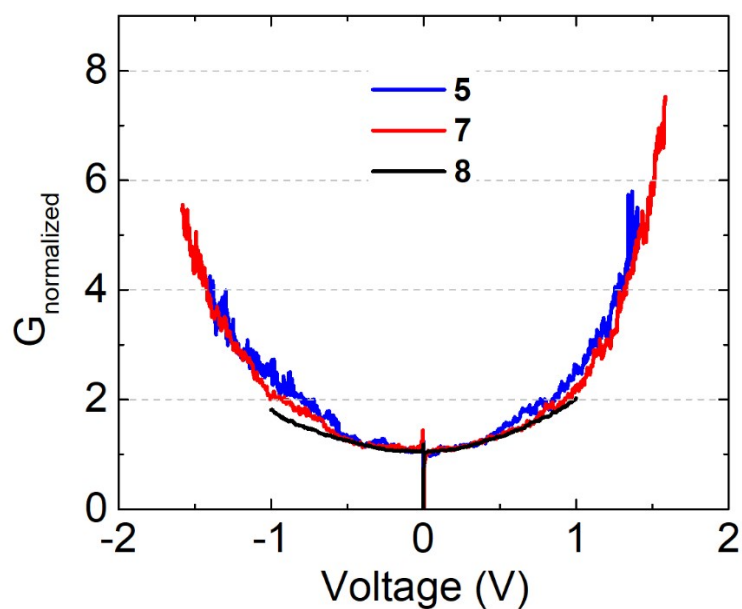


Figure S21. Normalised and averaged  $G$ - $V$  traces for compounds **5**, **7** and **8**.

## 10 Transport calculations

### 10.1 Technical details

We performed DFT-based transport calculations following the procedure described in detail in ref. [24, 25], which is based on the Turbomole code [26]. For this, a def-SVP basis set [27] and BP86 functional [28] were employed. Au-molecule-Au junctions were built by inserting the optimized structures of the gas phase molecules between two Au<sub>20</sub> pyramidal clusters and by performing a new optimization of the whole geometry. In this last step, the atoms in the two innermost gold layers and the molecule were relaxed while the others were kept frozen. This was followed by extending the size of each gold cluster to 63 atoms (to ensure correct charge transfer) and performing a single-point calculation on the new structure. The transport properties were then evaluated in the spirit of the Landauer formalism, after correcting the HOMO-LUMO gap with the DFT+ $\Sigma$  correction [25, 29]. The low-bias conductance was given by  $G = G_0 \tau(E_F) = G_0 \sum_i \tau_i(E_F)$ , where  $G_0$  is the conductance quantum  $2e^2/h$ ,  $E_F$  is the Fermi energy, and  $\{\tau_i\}$  are the transmission coefficients.

## 10.2 DFT-based results for pentalene versus dibenzopentalene cores

Molecule **5c** (Figure S22) was obtained replacing the DBP core in **5** with pentalene. Although such a structure would most likely be unstable if synthesised, it was studied theoretically to investigate the effect of having a more anti-aromatic core and thus useful as proof of concept. In Figure S22 (right-hand panel) the corresponding transmission curve is compared with that obtained for molecule **5b** (Figure S22 left-hand side - i.e. compound **5** minus the mesitylene side groups). Although the HOMO is positioned at higher energy for compound **5c** than for compound **5b**, this does not translate into an enhancement of the conductance. This can be explained due to the fact that the HOMO of **1c** is localized on the central pentalene unit only, and is thus weakly coupled to the leads (see Figure S23), and it also gives rise to interference originating from the interplay between all four double bonds. The overall effect is thus to lower the conductance. Conversely, in compound **5b** the corresponding orbital localized on the central DBP unit lies below the HOMO, and the HOMO is instead delocalized all over the entire molecule and contributes to an almost-Lorentzian resonance in the transmission curve. Thus, the lack of the same interference feature in the transmission curve of **5b** results in a higher conductance at the Fermi level compared to **5c**. Both compounds, however, have a higher conductance (at the Fermi level) than compound **8** with a phenyl ring at the core, which becomes more significant at higher energies closer to the LUMO levels.

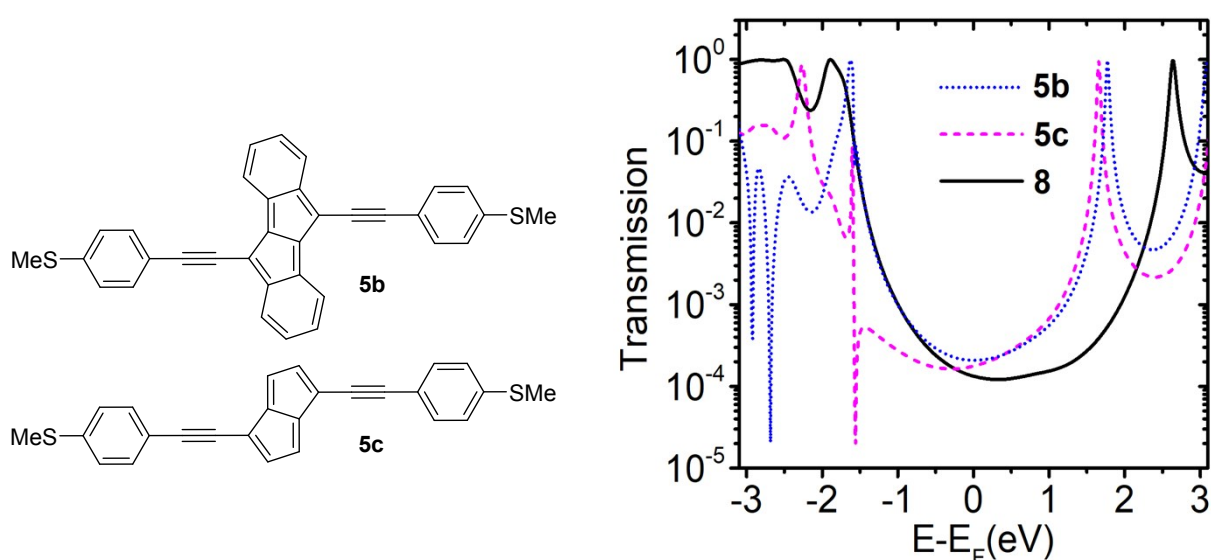


Figure S22. DFT-based transport results for compounds **5b** and **5c**.

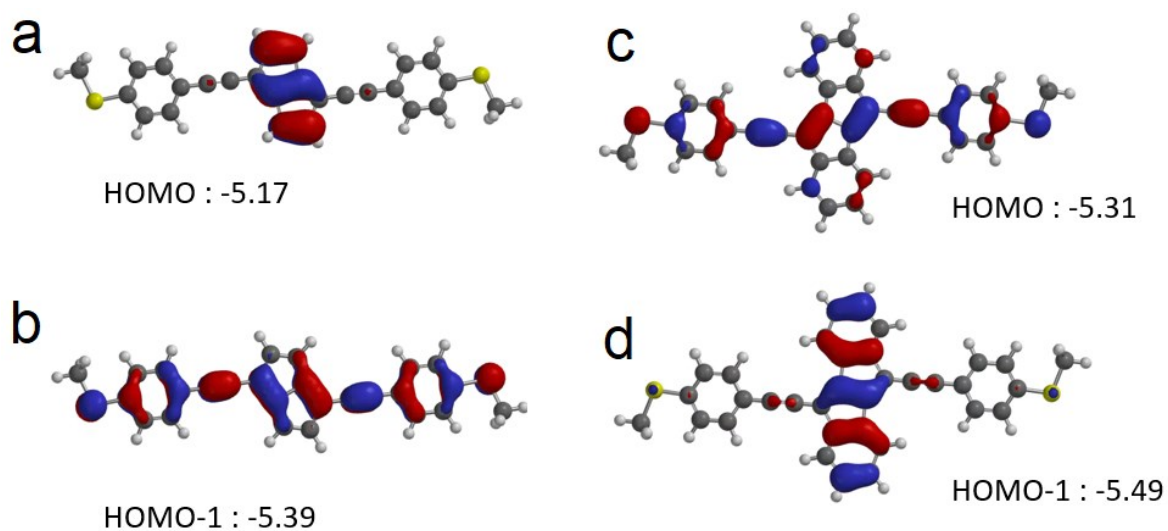


Figure S23. HOMO and HOMO-1 for compounds **5b** (right) and **5c** (left) from the gas-phase. Energies are given in eV.

### 10.3 Tight-binding transport calculations

Figure S24 shows the transmission curves obtained from a simple tight-binding model. Unless otherwise stated, all atoms in the backbone of each compound were included (except for the mesitylene side groups in **5** and **6**). The on-site energies and hopping parameters are given in the caption to Figure S24. The shape of each curve reproduces the DFT curves (shown in Fig 3b of the main text) well, highlighting that transport is dominated by the  $\pi$  system in each molecule.

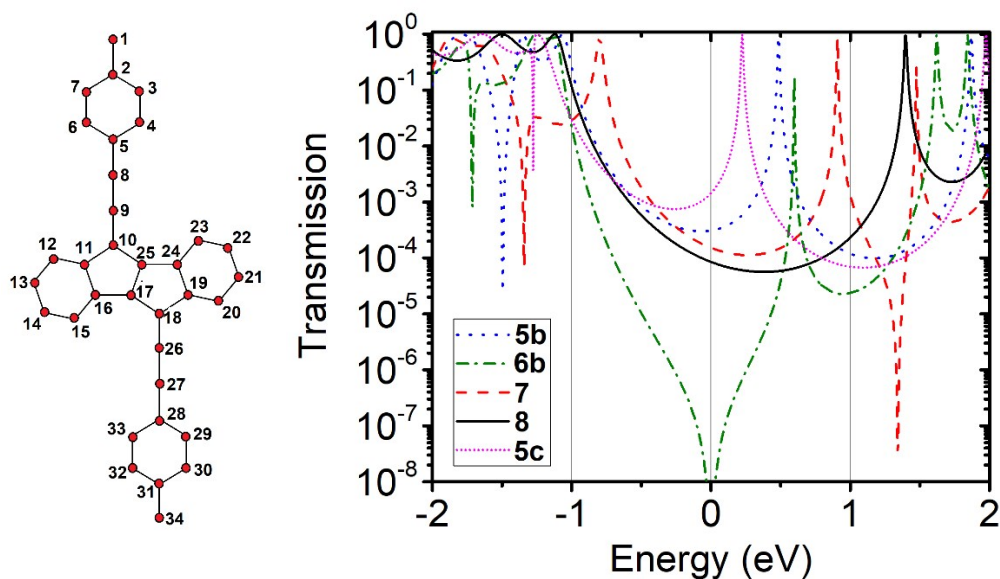


Figure S24. Tight binding results. (Left panel) A representation of the model used for **5b**. The parameters used were as follows: All on-site energies were set to 0 eV (except for sites 1 and 34, i.e. the binding groups, which were set to -2.8 eV). All phenyl ring couplings were set to -2.5 eV. Single bonds 5-8, 9-10, 18-26 and 27-28 were set to -2.0 eV. Triple bonds 8-9 and 26-27 were set to 2.8 eV. For the pentalene core, double bonds 10-25, 17-18 were set to 2.6 eV and single bonds 10-11, 16-17, 18-19 and 24-25 to 2.2 eV. The coupling to the electrodes ( $\Gamma_{L/R}$ ) was set to 0.5 eV. For compounds **5c**, **6b**, **7** and **8** all relevant parameters were kept identical.

## 11 A note on the relation between aromaticity/antiaromaticity and HOMO-LUMO gap.

The effect of aromaticity/antiaromaticity on HOMO-LUMO gap can be explained in terms simple molecular orbital theory. In the case of aromatic compounds, the interaction of each of the p-orbitals in the ring is overall stronger when compared with antiaromatics due to the preference for cyclic delocalization. The bond fixation which occurs in antiaromatic compounds results in significant bond length alternation and thus, while for neighbouring atoms the interaction may be strong, the overall interaction around the ring is lower w.r.t equivalent aromatics. The reduced interaction in the case of antiaromaticity leads to a lower (higher) LUMO (HOMO) and thus a reduction in HOMO-LUMO gap compared to linear olefinic analogues, that is to say an additional destabilization of bonding states and stabilization of antibonding states occurs, which is the reverse of the situation for aromatic compounds.

## 12 References

- [1] D. Bradley, G. Williams, M. Lawton, *J. Org. Chem* **2010**, *75*, 8351.
- [2] G. R. Fulmer, A. J. M. Miller, N. H. Sherden, H. E. Gottlieb, A. Nudelman, B. M. Stoltz, J. E. Bercaw, K. I. Goldberg, *Organometallics* **2010**, *29*, 2176–2179.
- [3] D. C. Grenz, M. Schmidt, D. Kratzert, B. Esser, *J. Org. Chem.* **2018**, *83*, 656–663.
- [4] J. Wilbuer, D. C. Grenz, G. Schnakenburg, B. Esser, *Org. Chem. Front.* **2017**, *4*, 658–663.
- [5] C. Dai, Z. Yuan, J. C. Collings, T. M. Fasina, R. L. Thomas, K. P. Roscoe, L. M. Stimson, D. S. Yufit, A. S. Batsanov, J. A. K. Howard, et al., *CrystEngComm* **2004**, *6*, 184–188.
- [6] *TURBOMOLE V7.3.1 2019, a Development of University of Karlsruhe and Forschungszentrum Karlsruhe GmbH, 1989-2007, TURBOMOLE GmbH, TURBOMOLE GmbH, Since 2007, 2007.*
- [7] G. E. S. M. J. Frisch, G. W. Trucks, H. B. Schlegel, V. B. M. A. Robb, J. R. Cheeseman, G. Scalmani, A. V. M. G. A. Petersson, H. Nakatsuji, X. Li, M. Caricato, H. P. H. J. Bloino, B. G. Janesko, R. Gomperts, B. Mennucci, D. W.-Y. J. V. Ortiz, A. F. Izmaylov, J. L. Sonnenberg, A. P. F. Ding, F. Lipparini, F. Egidi, J. Goings, B. Peng, N. R. T. Henderson, D. Ranasinghe, V. G. Zakrzewski, J. Gao, R. F. G. Zheng, W. Liang, M. Hada, M. Ehara, K. Toyota, H. N. J. Hasegawa, M. Ishida, T. Nakajima, Y. Honda, O. Kitao, J. E. P. T. Vreven, K. Throssell, J. A. Montgomery, Jr., et al., **2019**.
- [8] K. Eichkorn, O. Treutler, H. Öhm, M. Häser, R. Ahlrichs, *Chem. Phys. Lett.* **1995**, *240*, 283–290.
- [9] S. Grimme, J. Antony, S. Ehrlich, H. Krieg, *J. Chem. Phys.* **2010**, *132*, 154104.
- [10] S. Grimme, S. Ehrlich, L. Goerigk, *J. Comput. Chem.* **2011**, *32*, 1456–1465.
- [11] A. D. Becke, E. R. Johnson, *J. Chem. Phys.* **2005**, *123*, 154101.
- [12] E. R. Johnson, A. D. Becke, *J. Chem. Phys.* **2006**, *124*, 174104.
- [13] S. Grimme, J. G. Brandenburg, C. Bannwarth, A. Hansen, *J. Chem. Phys.* **2015**, *143*, DOI 10.1063/1.4927476.
- [14] M. Häser, R. Ahlrichs, H. P. Baron, P. Weis, H. Horn, *Theor. Chim. Acta* **1992**, *83*, 455–470.
- [15] G. A. Petersson, A. Bennett, T. G. Tensfeldt, M. A. Al-Laham, W. A. Shirley, J. Mantzaris, *J. Chem. Phys.* **1988**, *89*, 2193–2218.
- [16] M. Bühl, C. van Wüllen, *Chem. Phys. Lett.* **1995**, *247*, 63–68.
- [17] P. Von, R. Schleyer, C. Maerker, A. Dransfeld, H. Jiao, N. J. R. Van, E. Hommes, *Nucleus-Independent Chemical Shifts: A Simple and Efficient Aromaticity Probe*, **1996**.
- [18] B. D'Andrade, S. Datta, S. R. Forrest, P. Djurovich, E. Polikarpov, M. E. Thompson, *Org. Electron.* **2005**, *6*, 11–20.
- [19] *SAINT V8.37A, Bruker AXS, Madison, Wisconsin, USA, 2015.*

- [20] L. Krause, R. Herbst-Irmer, G. M. Sheldrick, D. Stalke, *J. Appl. Crystallogr.* **2015**, *48*, 3–10.
- [21] G. M. Sheldrick, *Acta Crystallogr. Sect. A Found. Adv.* **2015**, *71*, 3–8.
- [22] G. M. Sheldrick, *Acta Crystallogr. Sect. C Struct. Chem.* **2015**, *71*, 3–8.
- [23] C. B. Hübschle, G. M. Sheldrick, B. Dittrich, *J. Appl. Crystallogr.* **2011**, *44*, 1281–1284.
- [24] Pauly, F.; Viljas, J. K.; Huniar, U.; Häfner, M.; Wohlthat, S.; Bürkle, M.; Cuevas, J. C.; Schön, G. Cluster-Based Density-Functional Approach to Quantum Transport through Molecular and Atomic Contacts. *New J. Phys.* **2008**, *10* (12), 125019.
- [25] Zotti, L. A.; Bürkle, M.; Pauly, F.; Lee, W.; Kim, K.; Jeong, W.; Asai, Y.; Reddy, P.; Cuevas, J. C. Heat Dissipation and Its Relation to Thermopower in Single-Molecule Junctions. *New J. Phys.* **2014**, *16* (1), 015004.
- [26] Ahlrichs, R.; Bär, M.; Häser, M.; Horn, H.; Kölmel, C. Electronic Structure Calculations on Workstation Computers: The Program System Turbomole. *Chem. Phys. Lett.* **1989**, *162* (3), 165–169. (turbomole)
- [27] Schäfer, A.; Horn, H.; Ahlrichs, R. Fully Optimized Contracted Gaussian Basis Sets for Atoms Li to Kr. *J. Chem. Phys.* **1992**, *97* (4), 2571–2577. (basis)
- [28] Perdew, J. P. Density-Functional Approximation for the Correlation Energy of the Inhomogeneous Electron Gas. *Phys. Rev. B* **1986**, *33* (12), 8822. (functional)
- [29] Quek, S. Y.; Venkataraman, L.; Choi, H. J.; Louie, S. G.; Hybertsen, M. S.; Neaton, J. Amine– Gold Linked Single-Molecule Circuits: Experiment and Theory. *Nano Lett.* **2007**, *7* (11), 3477–3482.
- [30] Arroyo, C. R.; Leary, E.; Andrés Castellanos-Gómez, A.; Rubio-Bollinger, G.; González, M. T.; Agraït, N. *J. Am. Chem. Soc.* **2011**, *133*, 36, 14313–14319
- [31] J. Wilbuer, D. C. Grenz, G. Schnakenburg and B. Esser, *Org. Chem. Front.*, **2017**, *4*, 658–663.
- [32] D. C. Grenz, M. Schmidt, D. Kratzert and B. Esser, *J. Org. Chem.*, **2018**, *83*, 656–663.
- [33] M. Hermann, D. Wassy, D. Kratzert and B. Esser, *Chem. Eur. J.*, **2018**, *24*, 7374–7387.
- [34] M. Hermann, R. Wu, D. C. Grenz, D. Kratzert, H. Li and B. Esser, *J. Mater. Chem. C*, **2018**, *6*, 5420–5426.
- [35] D. Wassy, M. Pfeifer and B. Esser, *J. Org. Chem.*, **2020**, *85*, 34–43.